WP15ER-PR(18) 21046

SJP Pamela et al.

A wall-aligned grid generator for 3D non-linear simulations of MHD instabilities in tokamak plasmas

Preprint of Paper to be submitted for publication in
Computer Physics Communications

This work has been carried out within the framework of the EUROfusion Consortium and has received funding from the Euratom research and training programme 2014-2018 under grant agreement No 633053. The views and opinions expressed herein do not necessarily reflect those of the European Commission.

A wall-aligned grid generator for 3D non-linear simulations of MHD instabilities in tokamak plasmas

S.Pamela[1], G.Huijsmans[2,3], A.J.Thornton[1], A.Kirk[1], S.F.Smith[1,4], M.Hoelzl[5], T.Eich[5] and JET Contributors[6], the MAST Team[1] and the JOREK Team[7].

[*] *EUROfusion Consortium, JET, Culham Science Centre, Abingdon, OX14 3DB, UK.*
[1] *CCFE, Culham Science Centre, Abingdon, Oxon, OX14 3DB, UK.*
[2] *CEA, IRFM, F-13108 Saint-Paul-lez-Durance, France.*
[3] *Eindhoven University of Technology, Eindhoven, The Netherlands.*
[4] *York Plasma Institute, Department of Physics, University of York, Heslington, York YO10 5DD.*
[5] *Max-Planck-Institut für Plasmaphysik, Garching, Germany*
[6] *See author list of [X.Litaudon, Nucl. Fusion 57, 102001 (2017)].*
[7] *See https://www.jorek.eu team members.*

1 Introduction and Motivation

As fusion devices progress towards reactor-relevant conditions, the exhaust of particles and heat onto plasma facing components (PFCs) is acknowledged to be a major challenge [1]. In JET, the tungsten divertor is subject to damage in high power discharges, and there is growing concern that divertor heat loads will be one of the main restricting factors for operation capabilities in ITER [2]. Energy deposition on the divertor materials, due to steady-state heat fluxes as well as transient MHD events like Edge-Localised-Modes (ELMs), will be considerably increased in burning plasma experiments like ITER. Effectively most of the energy that crosses the separatrix into the Scrape-Off Layer (SOL) is transported along field lines to the divertor targets, and this effect is enhanced by increased heat conductivity at higher temperatures [3–5]. Combined with the large amplitude of these heat-fluxes, the longer duration of experimental pulses in reactor-sized devices will induce significant strain on the tungsten tiles, possibly leading to erosion and melting [6]. The tungsten tiles of the ITER divertor are designed to withstand up to $10\mathtt{MW.m}^{-2}$ in steady-state, and several thousands of transient events of up to $20\mathtt{MW.m}^{-2}$ [7, 8].

Ultimately, heat fluxes on PFCs are determined by how much energy escapes from the well-confined region inside the separatrix. It is well established that anomalous transport is responsible for this energy crossing the separatrix [9], and it is also well established that this occurs either in the form of turbulence filaments (blobs), or in the form of large-scale ELM filaments [10–13]. Hence, on one side, elaborate physics models (Fluid, MHD, drift-kinetic etc.) are indispensable to yield a robust understanding of anomalous transport in tokamaks. On the other side, the elaborate

geometry of magnetic equilibria, including X-point and separatrix, is a fundamental ingredient for the accurate description of filamentary transport at the plasma edge and in the SOL. This has led a number of state-of-the-art numerical codes [14–18] to use various field- or flux-aligned grid techniques, since it is essential to resolve the large parallel energy transport when these filaments cross the separatrix. However, the extension of such grids to the entire vacuum domain of a tokamak is not trivial, and often not undertaken.

In order to provide accurate estimates of divertor and first-wall heat-fluxes in present and future tokamak simulations, it is essential to consider the exact plasma domain inside the vacuum vessel wall. The precise location of individual wall components is necessary to obtain their respective heat-fluxes, and the accuracy of the global wall geometry is also required to represent the transport of neutral particles in various regions of the plasma domain. In addition, boundary conditions on wall components that are not aligned to magnetic field lines constitute a key aspect of simulations as a whole, particularly since Bohm and Sheath boundary conditions have a direct impact on the plasma dynamics in the entire SOL.

In this paper, we present the first results obtained using a new grid generator developed for the JOREK code [19, 20]. This new grid generator enables the extension of single and double X-point grids to the entire vacuum domain for arbitrary tokamak configurations. Simulations of ELMs are demonstrated using wall-extended grids for the JET-ILW tokamaks. Section-2 presents the JOREK code, including its bi-cubic Bezier finite-element formulation, and the visco-resistive MHD models used for simulations. Section-3 describes the methods used to extend flux-aligned grids to the first-vessel wall for arbitrary tokamak geometries. Section-4 discusses the use of Bohm Sheath boundary conditions [9] with wall-aligned grids. Section-5 shows initial results of ELM simulations in the JET-ILW tokamak, and discusses prospects for future studies with the new wall-extension grid generator in JOREK. This article is closed with a brief conclusion in Section-6.

2 The JOREK Code

2.1 Visco-resistive MHD with neutrals density

The 3D nonlinear MHD code JOREK was developed by Huysmans *et al.* with the specific aim to produce simulations of Edge-Localised-Modes [19, 21]. The MHD model used for the present paper is similar to that used in previous ELM and disruption studies [22, 23]. It is a six-field reduced MHD model for the variables ψ (poloidal magnetic flux), Φ (electric potential), $\vec{v}_{\|}$ (parallel velocity), ρ (ion density), T (total temperature), ρ_n (neutral density), including the two-fluid diamagnetic effects [24]. The reduction of the equations assumes that the perpendicular velocity lies in the poloidal plane, and that the toroidal magnetic field is constant in time, so that the total plasma velocity and the total magnetic field are expressed respectively as

$$\begin{aligned}\vec{\mathrm{v}}_{tot} &= \vec{\mathrm{v}}_{\parallel} + \vec{\mathrm{v}}_{\perp} = \vec{\mathrm{v}}_{\parallel} + \vec{\mathrm{v}}_{E} + \vec{\mathrm{v}}_{*i} \\ &= v_{\parallel}\vec{B} + R\vec{e}_{\phi} \times \nabla\Phi + \frac{\delta^* R}{\rho}\vec{e}_{\phi} \times \nabla p_i, \qquad (1)\\ \vec{B} &= \vec{B}_{\phi} + \vec{B}_{p} = \frac{F_o}{R}\vec{e}_{\phi} + \frac{1}{R}\nabla\psi \times \vec{e}_{\phi}, \qquad (2)\end{aligned}$$

where R is the major radius, $\vec{e}_\phi$ is the toroidal unit vector and $F_o = B_o R_o$, with B_o being the magnetic field amplitude at the reference major radius $R = R_o$. The diamagnetic component of the perpendicular velocity is represented by the third term $\vec{\mathrm{v}}_{*i} = \delta^* R\rho^{-1}\vec{e}_\phi \times \nabla p_i$, where p_i is the ion pressure and $\delta^* = (\Omega_{ci} R_o)^{-1}$, with the ion gyrofrequency $\Omega_{ci} = eB_o/m_i$. Substituting the identities (1) and (2) into the visco-resistive MHD equations gives the reduced MHD model, first derived by H.R. Strauss [25], with two separate equations for the parallel and the perpendicular momentum. The complete set of equations is as follows, where diamagnetic terms are highlighted in green, neutral density terms in red, and hyper-diffusive terms in blue:

$$\begin{aligned}\rho\tfrac{d\vec{\mathrm{v}}_E}{dt} = &- \rho\vec{\mathrm{v}}_{*i}\cdot\nabla\vec{\mathrm{v}}_E - \nabla_\perp p + \vec{J}\times\vec{B} + \mu\nabla^2(\vec{\mathrm{v}}_E + \vec{\mathrm{v}}_{*i}) \\ &+ \left(\rho^2\alpha_{rec} - \rho\rho_n S_{ion}\right)\vec{\mathrm{v}}_E + \mu_{hyp}\nabla^4\vec{\mathrm{v}}_E, \qquad (3)\\ \rho\tfrac{d\vec{\mathrm{v}}_\parallel}{dt} = &- \rho\vec{\mathrm{v}}_\parallel\cdot\nabla\vec{\mathrm{v}}_\parallel - \nabla_\parallel p + \mu\nabla^2\left(\vec{\mathrm{v}}_\parallel - V_{NBI}\right) \\ &+ \left(\rho^2\alpha_{rec} - \rho\rho_n S_{ion}\right)\vec{\mathrm{v}}_\parallel + \mu_{hyp}\nabla^4\vec{\mathrm{v}}_\parallel, \qquad (4)\\ \tfrac{\partial\psi}{\partial t} = &\ \eta(j - j_A) + R[\psi,\Phi] - \frac{\partial\Phi}{\partial\phi} \\ &- \frac{\delta^* R}{\rho}[\psi, p_e] + \frac{\delta^*}{\rho}\frac{\partial p_e}{\partial\phi} + \eta_{hyp}\nabla^2 j, \qquad (5)\\ \tfrac{\partial\rho}{\partial t} = &- \nabla\cdot\left(\rho\left[\vec{\mathrm{v}}_\parallel + \vec{\mathrm{v}}_E + \vec{\mathrm{v}}_{*i}\right]\right) + \nabla\cdot(D_\perp\nabla_\perp\rho) + S_\rho \\ &+ \left(\rho\rho_n S_{ion} - \rho^2\alpha_{rec}\right) + D_{hyp}\nabla^4\rho, \qquad (6)\\ \tfrac{\partial p}{\partial t} = &- \vec{\mathrm{v}}_E\cdot\nabla p - \gamma p\nabla\cdot\vec{\mathrm{v}}_E \\ &+ \nabla\cdot\left(\kappa_\perp\nabla_\perp T + \kappa_\parallel\nabla_\parallel T\right) + \frac{2}{3R^2}\eta j^2 + S_T \\ &+ \xi_{ion}\rho\rho_n S_{ion} - \rho\rho_n L_{lines} - \rho^2 L_{brem}, \qquad (7)\\ \tfrac{\partial\rho_n}{\partial t} = &\ \nabla\cdot\left(\vec{D}_n : \nabla\rho_n\right) + S_\rho - \left(\rho\rho_n S_{ion} - \rho^2\alpha_{rec}\right), \qquad (8)\\ & \qquad (9)\end{aligned}$$

where the density, temperature and current sources S_ρ, S_T and j_A have been introduced. The current source term j_A also includes the time-dependent bootstrap current calculated using Sauter's

formula [26]. The convective derivative, the parallel gradient, the perpendicular gradient, and the Poisson brackets are defined as

$$\begin{aligned}
&\frac{d}{dt} = \frac{\partial}{\partial t} + \vec{\mathtt{v}}_{_E} \cdot \nabla, \\
&\nabla_{\parallel} = \vec{b}\left[\vec{b} \cdot \nabla\right], \\
&\nabla_{\perp} = \nabla - \nabla_{\parallel}, \\
&[\alpha, \beta] = \vec{e}_{\phi} \cdot (\nabla\alpha \times \nabla\beta), \\
&\vec{b} = \frac{1}{|B|}\vec{B}.
\end{aligned}$$

As defined in [23], S_{ion} and α_{rec} are the ionization and recombination rate coefficients for deuterium, ξ_{ion} is the normalized ionization energy of a D atom (here set to 13.6 eV), and L_{lines} and L_{brem} are the line and bremsstrahlung radiation rate coefficients (based on ADAS data [27]).

Note that equations (3) and (4) can be reduced to scalar equations by projecting them in the poloidal and parallel directions, respectively, by applying the operators $\nabla \cdot [R\vec{e}_{\phi} \times ()]$ and $\vec{b} \cdot ()$. This reduced set of equations (without the diffusive transport terms and the diamagnetic terms) is equivalent to that derived by HR.Strauss, where energy of the system is shown to be conserved at first order [28, 29].

The perpendicular mass and thermal diffusivities $D_{\perp}$ and $\kappa_{\perp}$ used in simulations are ad-hoc coefficients with a well at the pedestal region to represent the H-mode transport barrier. Spitzer resistivity $\eta = \eta_o(T_e/T_{e,o})^{-3/2}$ is used, with $T_{e,o}$ the electron temperature at the magnetic axis. Likewise, a temperature-dependent perpendicular viscosity is used: $\mu = \mu_o(T_e/T_{e,o})^{-3/2}$. The Braginskii parallel thermal conductivity $\kappa_{\parallel}$ is expressed as $\kappa_{\parallel} = \kappa_{\parallel o}(T/T_o)^{5/2}$. The ratio of specific heat is $\gamma = 5/3$. Hyper-diffusive coefficients $\mu_{_{hyp}}$, $\eta_{_{hyp}}$ and $D_{_{hyp}}$ are also used in these simulations, but with values small enough not to influence the physics results. Typically, $\eta_{_{hyp}} \sim \eta^2$ is chosen (and similarly for $\mu_{_{hyp}}$ and $D_{_{hyp}}$).

The normalization of the equations is based on the magnetic permeability μ_o and the core density ρ_o, so that time is normalized to a near Alfven time $t = t_{_{SI}}/\sqrt{\mu_o\rho_o}$. For a deuterium plasma with particle density $n_o = 6 \times 10^{19}\mathtt{m}^{-3}$, a normalized time unit corresponds to approximately $0.5\mu\mathtt{s}$. Naturally, current is normalized with μ_o and density with ρ_o. Pressure is normalized with μ_o.

2.2 Spatial and Temporal Discretization

The spatial discretization of the JOREK code is made of a 2D grid in the poloidal plane, and a pseudo-spectral Fourier representation in the toroidal direction. The 2D poloidal grid is composed with isoparametric bi-cubic Bezier finite elements, as described in [21]. This finite element grid is aligned to equilibrium flux surfaces for the three regions of the core, the SOL and the private region. This alignment along flux surfaces is particularly important in the region of the separatrix, in order to treat accurately the fast parallel transport of energy along magnetic field lines.

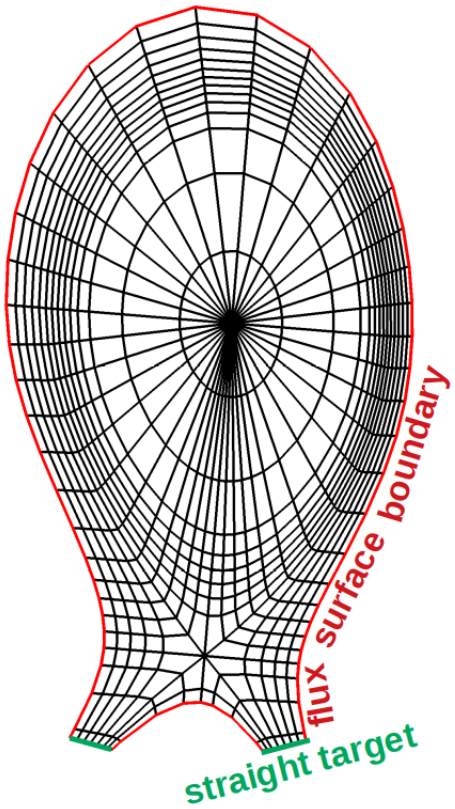

Figure 1: *A typical low-resolution JOREK grid with X-point. The domain boundaries are defined by flux surfaces in the SOL and the private regions, and by straight lines for the divertor targets.*

In previous studies, the edge of the simulation domain was generally defined as a flux surface in the SOL and private region, and a straight line for the target region, as shown in Figure-1. This domain configuration is robust as it ensures Mach-1 Bohm boundary conditions are only necessary on the target boundary.

The time stepping is done using the implicit Crank-Nicolson scheme, so that the size of time steps depends only on the time scale of the instabilities that are simulated. This implicit scheme results in a sparse system of equations, which is solved using a Generalized Minimal REsidual Solver (GMRES). The preconditioner for this iterative GMRES is obtained by solving independently each sub-matrix corresponding to different Fourier harmonics, which amounts to a block-Jacobi preconditioner. These sub-matrices are solved using the direct parallel sparse matrix solver PaStiX [30].

In order to allow the $n = 0$ component of the $\vec{E} \times \vec{B}$ and parallel flows to evolve towards a stationary equilibrium, the simulations are first run without toroidal modes, with only the equilibrium $n = 0$. This allows the Bohm boundary conditions to diffuse into the SOL. Note that at the zeroth time step, $\vec{v}_{\|}$ is Mach-1 on the target, and zero inside the plasma, already at the nodes adjacent to the boundary.

3 The Wall-Extension Grid Generator

In view of adressing immediate tokamak physics issues of various domains, ranging from divertor physics to plasma-wall interactions during disruptions, the grid generator of JOREK has been

generalised to allow the extension of a flux-aligned grid to any surrounding wall structures. The method developed for this purpose is described here to demonstrate its robustness.

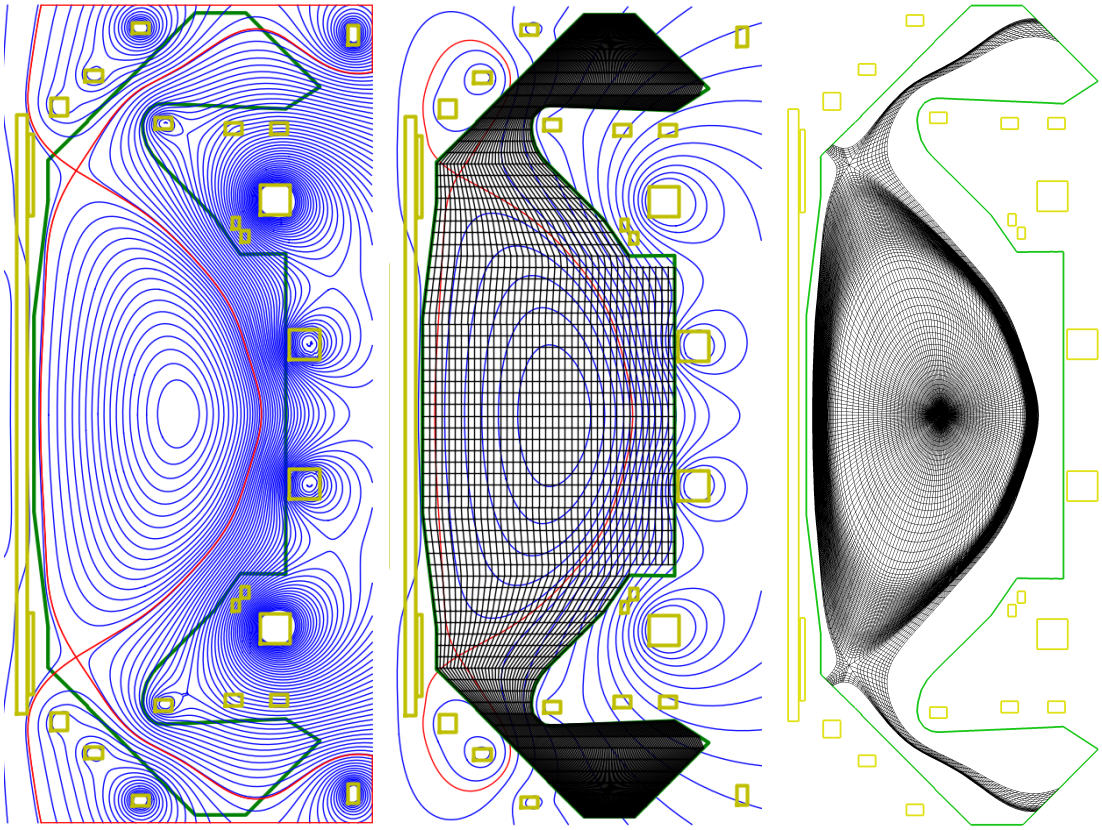

(a) (b) (c)

Figure 2:
(a) *Magnetic flux contours (blue) for a Super-X configuration of the MAST-U device. The connected double-null separatrix contour is shown in red, the first-wall in green, and the PF-coils in yellow.*
(b) *The initial rectangular grid on which the JOREK Grad-Shafranov equilibrium is solved, to obtain a flux-map consistent with ballooning unstable pre-ELM pressure profiles. For this Grad-Shafranov equilibrium, the boundary condition is the flux taken from the input equilibrium* (a)*. This initial rectangular grid is defined inside the first-wall, to avoid the necessity of taking PF-coil currents into account for the Grad-Shafranov equilibrium.*
(c) *The initial flux-aligned grid contained inside the first wall. This is the grid which can be extended. Note that a low-resolution grid is shown here for visual purpose.*

JOREK can take any input as initial Grad-Shafranov equilibrium, and use the exact pressure profile, FF' profile and ψ-map given from any equilibrium such as a geqdsk file from an EFIT++ equilibrium [31]. However, in some cases, particularly ELM studies, it is desirable to use different pressure and FF' profiles than the ones provided by external equilibrium solvers, to ensure that the initial equilibrium is unstable with respect to peeling-ballooning modes. In these cases, the ψ-map from the original equilibrium is often inconsistent with the new pressure profile, which results in a significant imbalance between the ∇p term and the $\vec{J} \times \vec{B}$ term of equation (3). This would result in an inherently unstable equilibrium. To ensure this balance is respected, JOREK solves its own Grad-Shafranov equilibrium internally.

In previous cases, as for Figure-1, a polar grid was used to solve the new Grad-Shafranov

equilibrium, for which the pressure and FF' profiles are given as input by the user, and the boundary condition for the solver is taken as the ψ-values of the original equilibrium data along the contour of this polar grid. The final flux-aligned grid is then built using the new equilibrium calculated on this polar grid. In the present case, since we aim at building a grid that extends to the wall, instead of a polar grid, a rectangular grid is built inside the first-wall, as shown in Figure-2b. This is convenient as it allows the Grad-Shafranov solver to ignore all PF-coil currents outside the wall.

Before extending a grid to the surrounding wall, we must build an initial grid inside that wall. This is done in a similar manner as in Figure-1, where the target must be aligned to the wall. An example of such initial grids is shown in Figure-2c, for a MAST-U Super-X configuration. Since the JOREK grid is composed of quadrilateral elements, an extension of a given grid must be composed of a number of quadrilaterals. Thus, the wall-extended grid is built simply by adjoining additional quadrilateral grid patches to the initial grid.

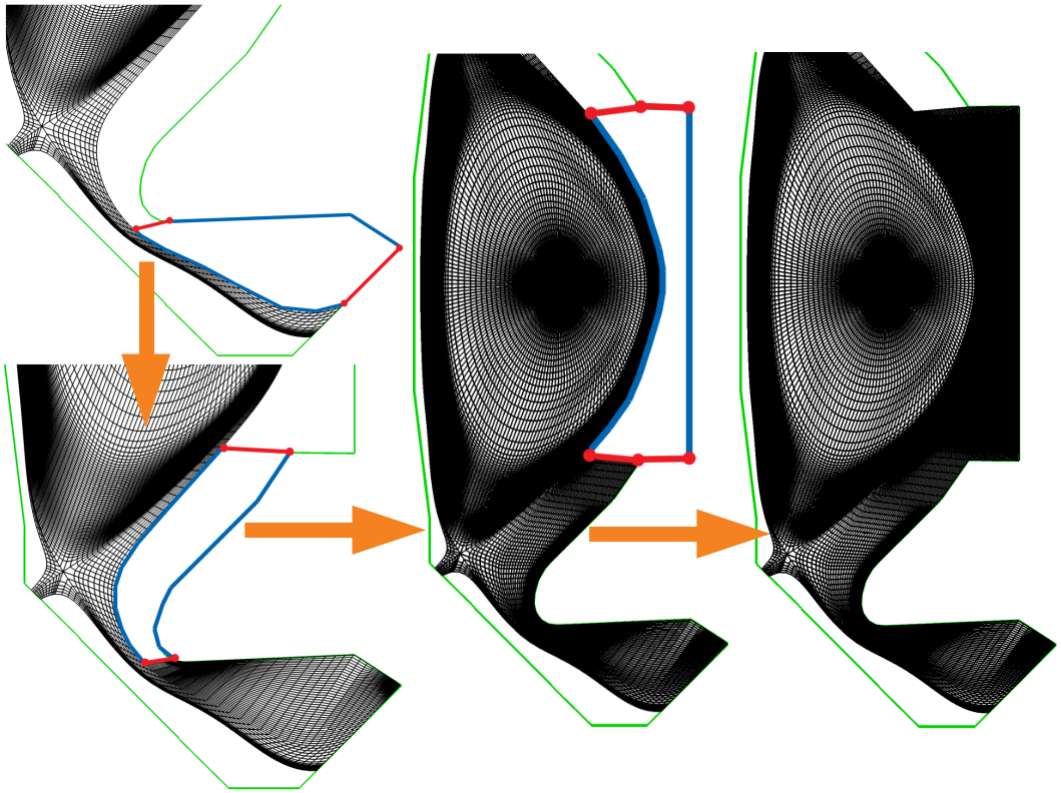

Figure 3: *An example of successive grid patches applied between the flux-aligned X-point grid and the wall. Grid extension patches need to be quasi-quadrangles, but do not need to have linear sides. The user specifies the sides of the patch (red lines) using a set of input points (red points). The grid generator then automatically extends the grid between the grid side and the wall side (blue lines).*

The flexibility of Bezier elements allows for grid patches to have non-linear sides, including curves and angles. The idea of the new generator is that the user can provide near-quadrilateral patches between the initial grid and the wall. This is done by specifying the two sides of each patch, between the grid and the wall, like the red lines in Figure-3. Note that these side can be

composed of multiple lines. The other two sides of the patch are determined automatically, along the grid, and along the wall, like the blue lines in Figure-3. The only requirement is that successive patches need to have matching sides. To ensure a smooth transition between the initial grid and the patches, the radial distribution of elements for the patches is automatically adapted such that their radial resolution at the junction matches that of the initial grid. Of course, the user can also specify the radial resolution of the new patches, but the poloidal resolution, however, is determined by the initial grid. In the case of matching successive patches, as in Figure-3, the radial resolution of the first patch determines the radial resolution of the following patches. Note that this patching method can be used any number of times, such that new grid patches can also be added on top of previous grid patches, which enables the description of complex wall structures, such as corners or isolated vacuum regions.

This grid-extension method is generic and robust enough that it may be applied to any toroidally axisymmetric tokamak device. Figure-4 shows examples of extended grids for MAST-U, JET-ILW and JT-60SA, which all have very different wall contours and separatrix shapes.

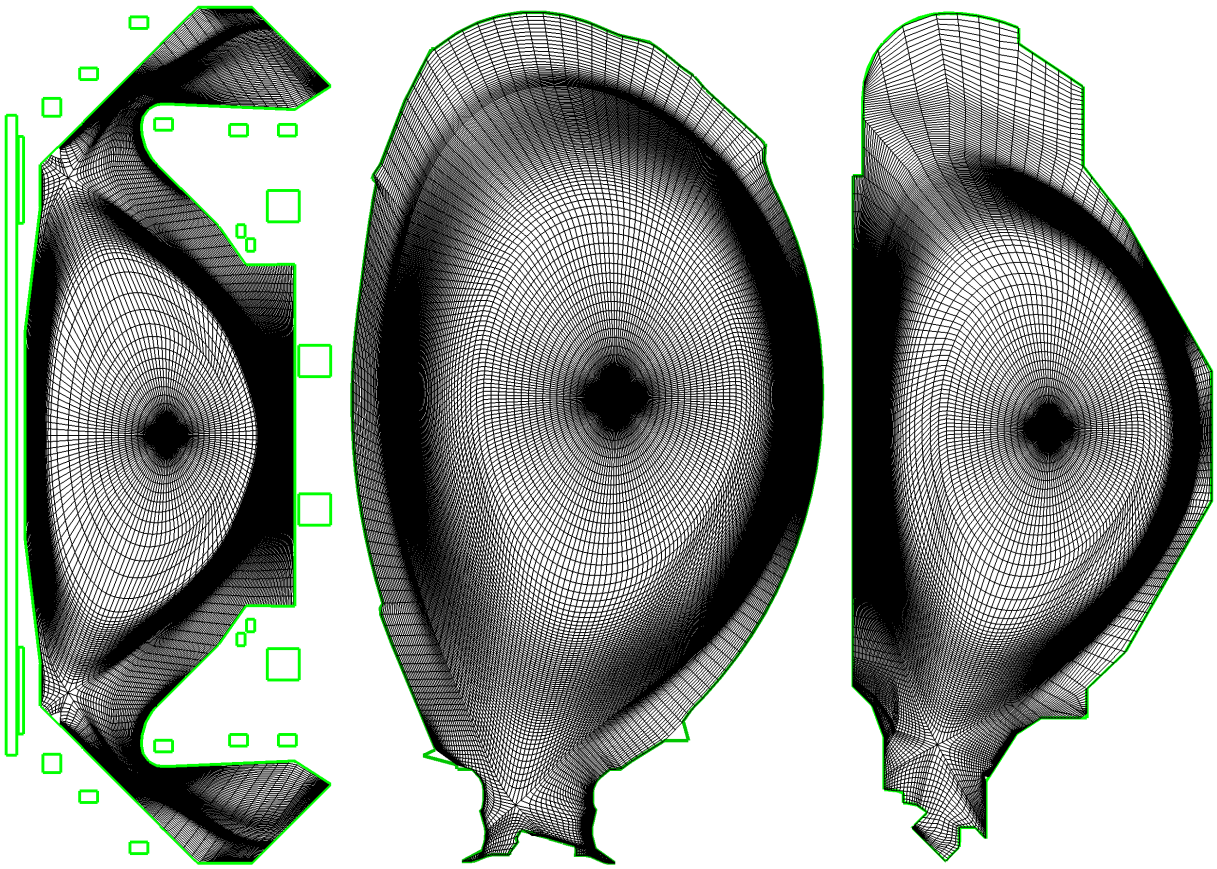

(a) (b) (c)

Figure 4: *Examples of wall-extended grids for three devices:* (a) *MAST-U,* (b) *JET-ILW and* (c) *JT-60SA.*

4 Sheath Boundary Conditions with a Wall-aligned Grid

With this new wall-extended grid, appropriate boundary conditions are required. The usual case is that magnetic field lines are incident to the boundary surfaces, thus requiring Bohm (Mach-1) and Sheath boundary conditions. These are expressed as:

$$\vec{v}_{tot} \cdot \vec{n} = \pm \; c_s = \pm \; \sqrt{\gamma T} \;\; \vec{b} \cdot \vec{n}, \tag{10}$$

$$nT\vec{v}_{\parallel} + \kappa_{\parallel} \nabla_{\parallel} T = \gamma_{sh} nT \vec{v}_{\parallel}. \tag{11}$$

where $\vec{n}$ is the unit vector normal to the boundary, $\vec{b}$ is the unit vector along the magnetic field, $\gamma = 5/3$ and $\gamma_{sh} = 4.5$. In the standard model, without neutrals density, density and temperature have free outflow boundary conditions at the target (no density reflection). However, when using the neutrals density model, as described above, a reflective coefficient ξ_{re} can be applied at the boundary, such that density arriving at the target is (fully or partly) reflected as neutrals into the simulation domain, as in [32]:

$$D_n \nabla \rho_n \cdot \vec{n} = - \; \xi_{re} \;\; \rho \vec{v}_{\parallel} \cdot \vec{n}, \tag{12}$$

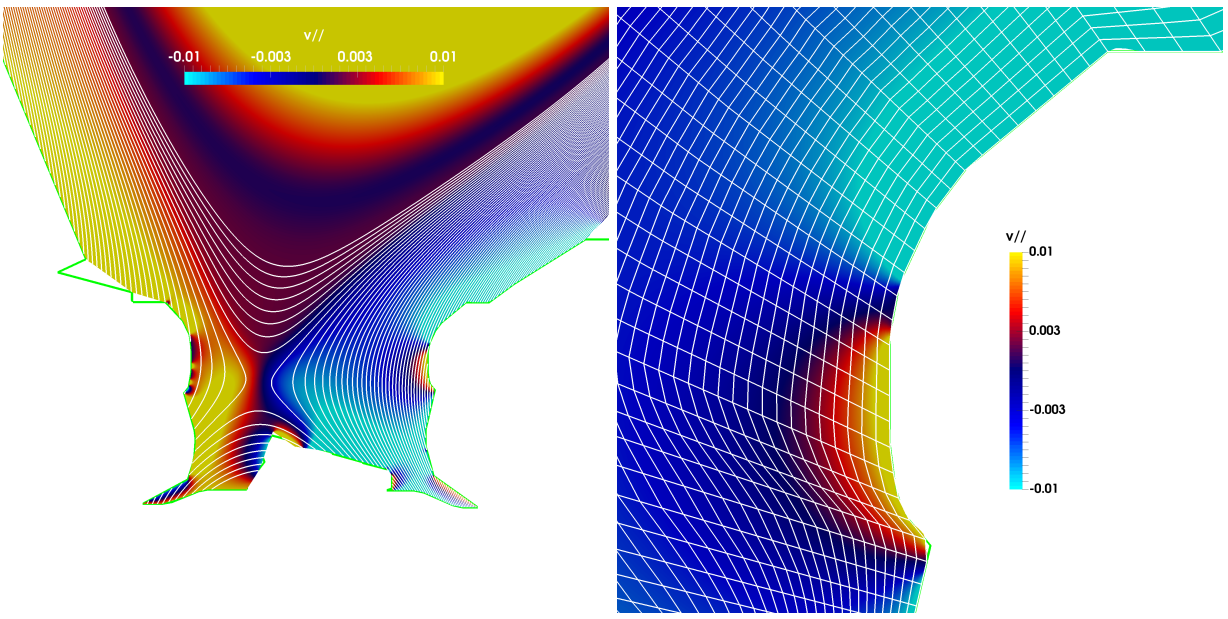

(a) (b)

Figure 5:
(a) *The direction of Mach-1 boundary conditions is determined by the direction of field lines going in/out of the domain boundary, which can change along the wall,*
(b) *The change in direction of the Mach-1 boundary condition can occur within a few elements.*

It should be noted that the direction of the magnetic field may change as we step along the boundary of the domain, going from positive, across zero, and negative. This is illustrated in Figure-5. It implies that the Mach-1 boundary condition can reverse direction within a grid element. A

threshold is used for the application of Mach-1 boundary conditions, which requires that the angle α between the magnetic field and the boundary is larger than 3°, which is approximately twice the lower limit given by Geraldini *et al.* [33]:

$$\sqrt{\frac{m_e}{m_i}} \ll \alpha \ll 1 \tag{13}$$

Even with relatively low parallel viscosity for equation-4, simulations remain numerically stable. In the ELM simulation presented in the next section, a spacially uniform value of $\mu_{\parallel} = 10^{-6} kg \cdot m^{-1} \cdot s^{-1}$ was used.

5 Prospects of Physics Applications with Wall-extended Grids

First-wall and divertor heat-fluxes

In order to demonstrate the ability of the new wall-extension grid-generator to handle non-linear simulations of large type-I ELM crashes, a type-I ELMy H-mode experiment of JET-ILW has been used. Pulse JPN-83334, which was thoroughly simulated and analysed in [22], is a 2.4T, 2.4MA, low-triangularity plasma, with 25MW of NBI heating, and with the outer strike point positioned on the main (bulk) tungsten divertor tile. The pre-ELM pedestal electron density and temperature are $5 \cdot 10^{19} m^{-3}$ and $1.2 keV$ respectively. For this test simulation, relatively high MHD parameters were used: a resistivity 200 times higher than $\eta_{spitzer}$, and a viscosity of $10^{-6} kg \cdot m^{-1} \cdot s^{-1}$, and diamagnetic effects are not included. The toroidal resolution used was $n = 2, 4, 6, 8, 10$. More challenging simulations with the wall-extended domain, using higher toroidal resolutions and more challenging diffusive parameters, will be the focus of future research in the coming years.

The energy loss of this simulated ELM is 3.9% of the total plasma energy content, which is reasonably close to the experimental value of 4.6% (averaged of all ELMs in the discharge). The peak heat-flux on the divertor target reaches just above $380 MW.m^{-2}$, which is also close to the experimental value of $360 MW.m^{-2}$ (also averaged over all ELMs). Note that, while reasonable agreement is achieved between this simulation and the corresponding experiment, the purpose of this work is not to validate the JOREK simulations (which would require diamagnetic effects as well as lower resistivity and viscosity), but rather to demonstrate the robustness of the new wall-extended grid and its applicability to simulations of type-I ELM instabilities. Figure-6a shows the parallel heat-flux for a snapshot of this simulation, while Figure-6b shows the temperature of the first wall at this same snapshot.

Divertor configurations, gas-fueling, and detachment

One of the main interests of providing an accurate description of the first-wall boundary in JOREK simulations is to enable the simulation of various gas-puffing levels as well as divertor configurations. As described in [34], JET-ILW experiments have demonstrated the importance of gas-puffing levels regarding ELM dynamics as well as global confinement levels. Similarly, the separatrix position

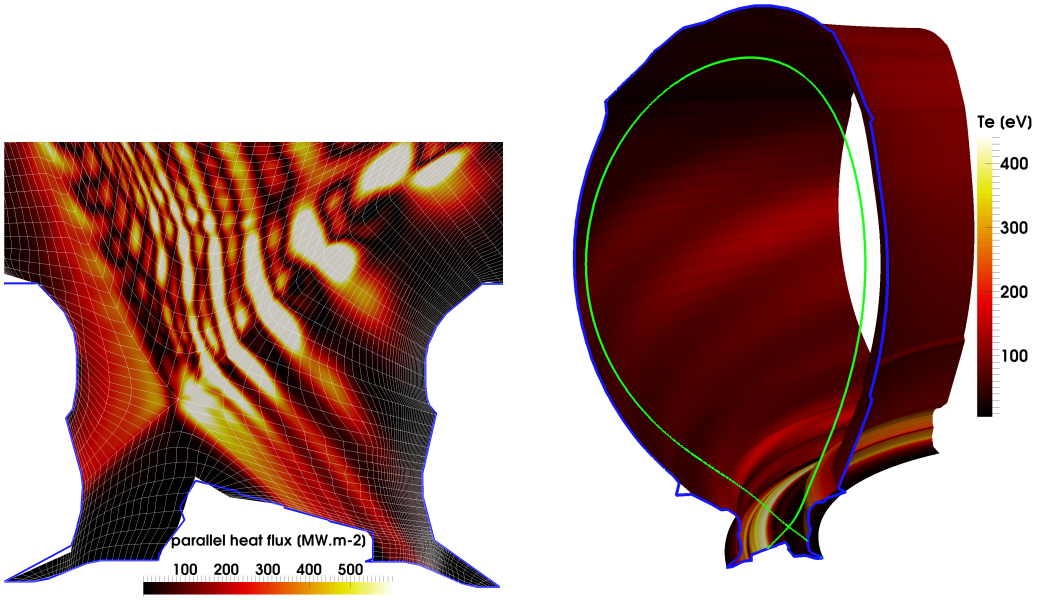

(a) (b)

Figure 6:
(a) *The parallel heat-flux amplitude in a JET-ILW ELM simulation,*
(b) *The electron temperature T_e [eV] on the wall during an ELM simulation in JET-ILW.*

with respect to the gas-injection valves and the divertor pumps plays a major role in neutrals dynamics and, as a consequence, pedestal performance in JET-ILW experiments [35].

Although the neutrals model described in section-2.1 and in [23] may not be sufficient to fully describe the complete neutrals dynamics in the SOL of JET-ILW (or other devices), it could provide a preliminary insight into the effect of SOL neutrals levels on pedestal and ELM physics. Figure-7 shows a test simulation of an ELM using the full model described in Section-2.1. The interaction of plasma filaments with the neutrals background is clearly visible in the upper SOL region.

Further work is under way to benchmark JOREK simulations of neutrals simulations with SOLPS [36], particularly addressing simulations of detachment and ELM burn-through in the new MAST-U device [37]. As shown in Figure-4a, the detailed description of the entire plasma domain enables the representation of increased neutrals pressure inside the closed divertor leg, crucial for detachment studies, as well as the computation of heat-fluxes on the nose of the divertor (where the outer wall almost reaches the outer leg, just below/above the X-points). However, this is a continuing effort which is left for future publications. In addition, a project is underway to add kinetic neutrals as particles [38].

Wall currents during disruptions

At last, development is ongoing to combine this new grid-generator with the emerging capabilities of the JOREK-STARWALL code in terms of disruption studies [39]. The final goal of detailed 3D tiled-wall representation, to provide precise calculations of hiro and halo currents, is a long-term

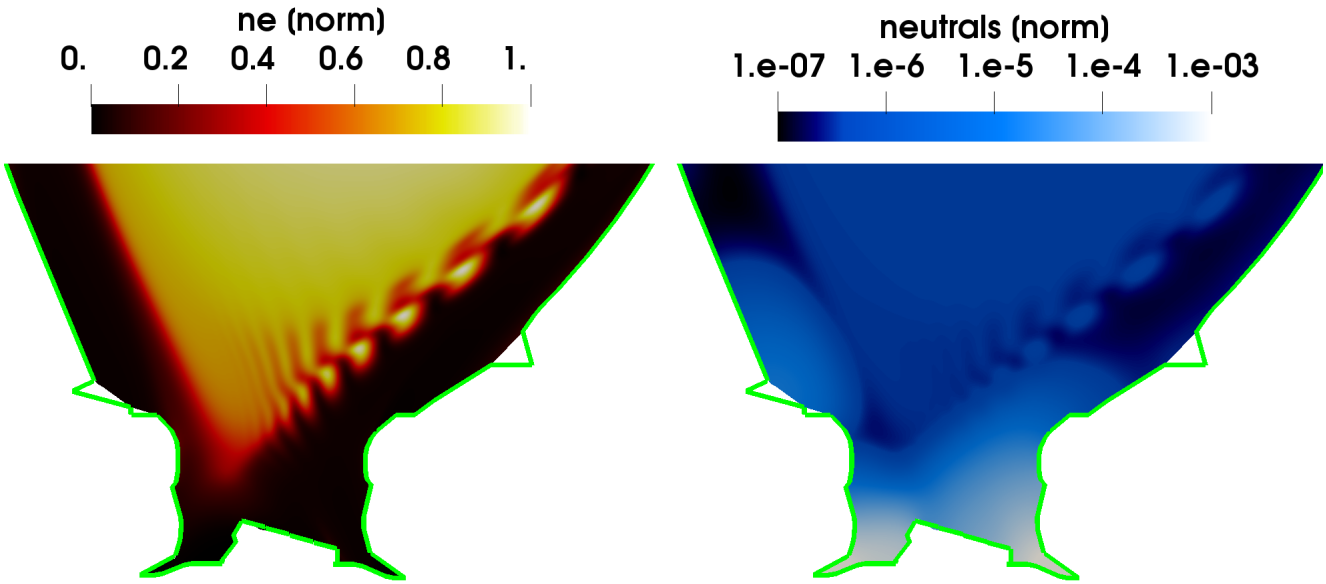

Figure 7: *A simulation of ELM filaments using the neutrals density model with divertor reflection of neutrals. Electron density (left) and neutrals density (right) are shown in the divertor region. Both quantities are normalised to the central* n_e *value:* $0.65 \times 10^{20} m^{-3}$.

challenge, and one of ITER's most pressing open physics issues. This wall-extended grid-generator provides a considerable step forward on the path towards this goal.

6 Summary and Future Studies

A new grid generator has been developed for the JOREK code, enabling any equilibrium to be meshed, including the entire plasma domain, all the way to the first wall. The appropriate fluid boundary conditions are applied to all wall surfaces, providing a detailed description of SOL flows. This paper demonstrates the practical feasibility of building grids for various tokamak devices, and an advanced JET-ILW ELM simulation shows the robustness of such new grids when used for state-of-the-art non-linear MHD simulations.

The wide range of physics areas accessible with this new grid generator is duplicated by its coupling with the JOREK neutrals density model. Advanced studies of divertor, SOL and pedestal physics, including detachment, ELM burn-through and impurity transport, can now be done in a detailed and systematic manner. It also contributes a significant step towards the full 3D description of plasma-wall interactions in disruption studies, one of ITER's urgent concerns. At last, this improvement enables direct comparisons of simulations with current experiments, as shown in Figure-8.

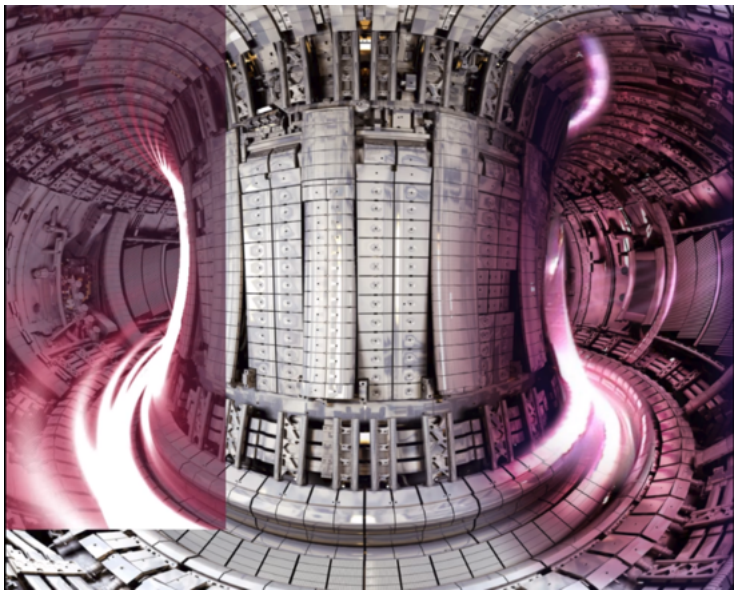

Figure 8: *A synthetic diagnostic of JET fast-visible camera for a JOREK ELM simulation (left), compared to an experiment (right).*

Acknowledgement

This work has been carried out within the framework of the EUROfusion Consortium and has received funding from the Euratom research and training programme 2014-2018 under grant agreement No 633053, and from the RCUK Energy Programme [grant number EP/I501045]. To obtain further information on the data and models underlying this paper please contact PublicationsManagerccfe.ac.uk. This work used the HELIOS supercomputer (IFERC-CSC), Japan, under the Broader Approach collaboration, implemented by Fusion for Energy and JAEA. The views and opinions expressed herein do not necessarily reflect those of the European Commission or the ITER Organization. The HEC ARCHER computer (UK), as part of the Plasma HEC Consortium EPSRC grant EP/L000237/1, and the MARCONI computer at CINECA in Italy, were also used.

References

[1] A.S. Kukushkin et al. A. Loarte, B. Lipschultz. *Nucl. Fusion 47, S203-S263*, 2007.

[2] J.W. Coenen et al. *Journal of Nuclear Materials 463, 78-84*, 2015.

[3] J.A. Goetz et al. *Phys. Plasmas 6, 1899*, 1999.

[4] S.I. Braginskii. *Review of Plasma Physics Vol.1, Ed M.A. Leontovitch (New York: Consult. Bureau) p205*, 1965.

[5] R. Goldston. *Phys. Plasmas 17, 012503*, 2010.

[6] A. Scarabosio et al. T. Eich, B. Sieglin. *Phys. Rev. Lett. 107, 215001*, 2011.

[7] R.A. Pitts et al. *Journal of Nuclear Materials 438, S48-S56*, 2013.

[8] M. Merola. *Journ. Nucl. Materials 2, 307-311, 1524-1532*, 2002.

[9] P.C. Stangeby. *The Plasma Boundary of Magnetic Fusion Devices, Institute of Physics Publishing*, 2000.

[10] A. Kirk et al. *Plasma Phys. Contr. Fusion 48*, 2006.

[11] B. Dudson et al. *Plasma Phys. Contr. Fusion 50*, 2008.

[12] S.J. Zweben et al. *Plasma Phys. Control. Fusion 49, S1-S23*, 2007.

[13] S.J. Zweben et al. *Nucl. Fusion 44, 134-153*, 2004.

[14] B.D. Dudson and J.Leddy. *Plasma Phys. Control. Fusion 59, 054010*, 2017.

[15] R.Schneider et al. *Contrib. Plasma Phys. 46, 3*, 2006.

[16] P.Tamain et al. *J. Comp. Phys. 321, 606-623*, 2016.

[17] C.S.Chang et al. *J. Phys.: Conference Series 180, 012057*, 2009.

[18] A.Stegmeir et al. *Plasma Phys. Control. Fusion 60, 035005*, 2018.

[19] G.T.A.Huysmans and O.Czarny. *Nucl. Fusion 47, 659*, 2007.

[20] G.T.A.Huijsmans and A.Loarte. *Nucl. Fusion 53, 123023*, 2013.

[21] O.Czarny and G.T.A.Huysmans. *J. Computational Phys. 227, 7423*, 2008.

[22] S.Pamela et al. *Nucl. Fusion 57, 076006*, 2017.

[23] A.Fil et al. *Physics of Plasmas 22, 062509*, 2015.

[24] F.Orain et al. *Phys. Plasmas 20, 102510*, 2013.

[25] H.R. Strauss. *Phys. Fluids 19, 134*, 1976.

[26] O.Sauter et al. *Phys. Plasmas 6, 7*, 1999.

[27] H.P.Summers. *http://adas.ac.uk, Atomic Data and Analysis Structure User Manual.*

[28] H.R. Strauss. *J. Plasma Physics, Vol. 57, part 1, pp 83-87*, 1997.

[29] E.Franck et al. *ESAIM:M2AN 49, 5, https://doi.org/10.1051/m2an/2015014*, 2015.

[30] P. Henon et al. *Parallel Comp. 34 345-362*, 2008.

[31] L.Appel et al. *Computer Physics Communications 223, 1-17*, 2018.

[32] M.Verbeek et al. *43rd EPS Conference Proceedings, P5.058*, 2016.

[33] A.Geraldini et al. *Plasma Phys. Control. Fusion 59, 025015*, 2017.

[34] C.Maggi et al. *Nucl. Fusion 55, 113031*, 2015.

[35] E.Joffrin et al. *Nucl. Fusion 57, 086025*, 2017.

[36] D.Moulton et al. *Plasma Phys. Control. Fusion 59, 065011*, 2017.

[37] S.Smith et al. *45th EPS conference, Prague, Czech Republic*, 2018 http://ocs.ciemat.es/EPS2018PAP/pdf/P4.1061.pdf.

[38] D. Van Vugt et al. *45th EPS conference, Prague, Czech Republic*, 2018 http://ocs.ciemat.es/EPS2018PAP/pdf/P1.1049.pdf.

[39] M.Hoelzl et al. *Journal of Physics: Conference Series 401, 012010*, 2012.